A Simple Method for 3D Analysis of Immunolabeled Axonal Tracts in a Transparent Nervous System

Morgane Belle, David Godefroy, Chloé M Dominici, Céline Heitz-Marchaland, Pavol Zelina, Farida Hellal, Frank Bradke, Alain Chedotal

Report

Cell Reports

A Simple Method for 3D Analysis of Immunolabeled Axonal Tracts in a Transparent Nervous System

Graphical Abstract

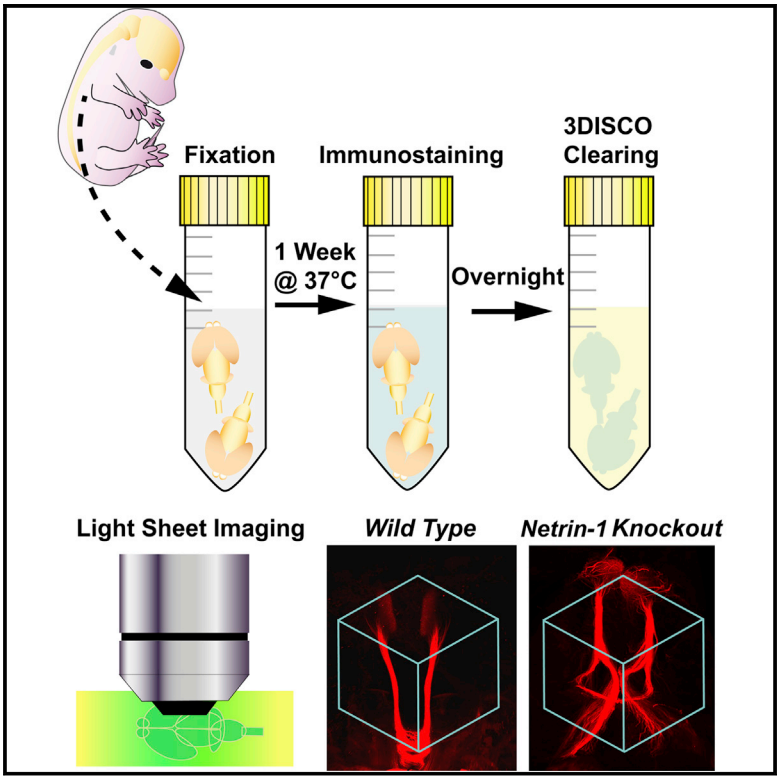

Highlights

Immunostaining and 3DISCO clearing: a powerful method for studying brain connections

3D analysis of axon guidance defects in midline mutant mice

Unexpected roles for Slits and Netrin-1 in fasciculus retroflexus development

Authors

Morgane Belle, David Godefroy, ..., Frank Bradke, Alain Chédotal

Correspondence

alain.chedotal@inserm.fr

In Brief

Clearing techniques have recently been developed to look at mouse brains, but they are complex and expensive. Belle et al. now describe a simple procedure that combines immunolabeling, solvent-based clearing, and light-sheet fluorescence microscopy. This technique allows large-scale screening of axon guidance defects and other developmental disorders in mutant mice.

Belle et al., 2014, Cell Reports 9, 1191–1201
November 20, 2014 ©2014 The Authors
http://dx.doi.org/10.1016/j.celrep.2014.10.037

Cell Reports
Report

A Simple Method for 3D Analysis of Immunolabeled Axonal Tracts in a Transparent Nervous System

Morgane Belle,[1,2,3,5] David Godefroy,[1,2,3,5] Chloé Dominici,[1,2,3] Céline Heitz-Marchaland,[1,2,3] Pavol Zelina,[1,2,3] Farida Hellal,[4,6] Frank Bradke,[4] and Alain Chédotal[1,2,3,*]
[1]Sorbonne Universités, UPMC Université Paris 06, UMRS 968, Institut de la Vision, Paris 75012, France
[2]INSERM, UMRS 968, Institut de la Vision, Paris 75012, France
[3]CNRS, UMR 7210, Paris 75012, France
[4]Deutsches Zentrum für Neurodegenerative Erkrankungen (DZNE), Axon Growth and Regeneration, Ludwig-Erhard-Allee 2, 53175 Bonn, Germany
[5]Co-first author
[6]Present address: Institute for Stroke and Dementia Research (ISD), Experimental Stroke Research, Max-Lebsche Platz 30, 81377 Munich, Germany
*Correspondence: alain.chedotal@inserm.fr
http://dx.doi.org/10.1016/j.celrep.2014.10.037

SUMMARY

Clearing techniques have been developed to transparentize mouse brains, thereby preserving 3D structure, but their complexity has limited their use. Here, we show that immunolabeling of axonal tracts followed by optical clearing with solvents (3DISCO) and light-sheet microscopy reveals brain connectivity in mouse embryos and postnatal brains. We show that the Robo3 receptor is selectively expressed by medial habenula axons forming the fasciculus retroflexus (FR) and analyzed the development of this commissural tract in mutants of the Slit/Robo and DCC/Netrin pathways. Netrin-1 and DCC are required to attract FR axons to the midline, but the two mutants exhibit specific and heterogeneous axon guidance defects. Moreover, floor-plate-specific deletion of Slit ligands with a conditional Slit2 allele perturbs not only midline crossing by FR axons but also their anteroposterior distribution. In conclusion, this method represents a unique and powerful imaging tool to study axonal connectivity in mutant mice.

INTRODUCTION

3D imaging of solvent-cleared organ (3DISCO) is a simple solvent-based clearing method used for transparentizing the brain of adult transgenic mice expressing fluorescent proteins such as GFP (Ertürk et al., 2012a) and Alexa-conjugated axonal tracers (Ertürk et al., 2012a, 2012b). In combination with light-sheet fluorescence microscopy (LSM), 3DISCO allows one to quickly generate 3D images of axonal tracts (Dodt et al., 2007; Ertürk et al., 2012a, 2012b). However, the fluorescence of GFP and related proteins rapidly vanishes after clearing. A handful of clearing methods using solvent-free reagents have since been described with which the fluorescence is better preserved (Chung et al., 2013; Hama et al., 2011; Ke et al., 2013; Susaki et al., 2014; Yang et al., 2014), but they are more complex technically. Clearing takes several days or even weeks and requires large volumes of expensive reagents, such as polymers, that impregnate the samples. Moreover, the number of fluorescent mouse lines that have been validated with these methods is still limited (in most cases, only Thy1-YFP transgenic lines were tested), and in any case, using them to study axonal projections in mutant mice would require time-consuming intercrosses. Therefore, we reasoned that there was still a need for simple, rapid, and inexpensive methods to clear and image brain samples.

We first thought that performing whole-mount immunostaining prior to clearing could be a good strategy, as this would alleviate the use of fluorescent reporters. Immunostaining is compatible with clarity (Chung et al., 2013), CUBIC (Susaki et al., 2014), and PACT (Yang et al., 2014) but is performed after clearing and therefore lengthens these procedures. We show here that 3DISCO clearing can be performed after whole-mount immunostaining on embryo or postnatal brain and preserves the activity of fluorescent dyes for several months. We also show that Robo3, a receptor of the roundabout family (Sabatier et al., 2004), is a unique marker of medial habenula (mHb) axons, which extend through the fasciculus retroflexus (FR) to the interpeduncular nucleus (IPN; Beretta et al., 2012). The FR exists in all vertebrate embryos (Figdor and Stern, 1993) and primarily targets the IPN, an unpaired structure extending across the ventral midline at the midbrain/hindbrain boundary (Beretta et al., 2012). FR axons pathfinding in the thalamus is controlled by Sema3F/Neuropilin-2 repulsion (Chen et al., 2000; Sahay et al., 2003). In vertebrates, the behavior of FR axons at the ventral midline is rather unique, as they cross it multiple times (Ramon y Cajal, 1911; Bianco et al., 2008; Iwahori et al., 1993). Surprisingly, the role of guidance cues such as Slits and Netrin-1 in midline crossing of FR axons had not been studied.

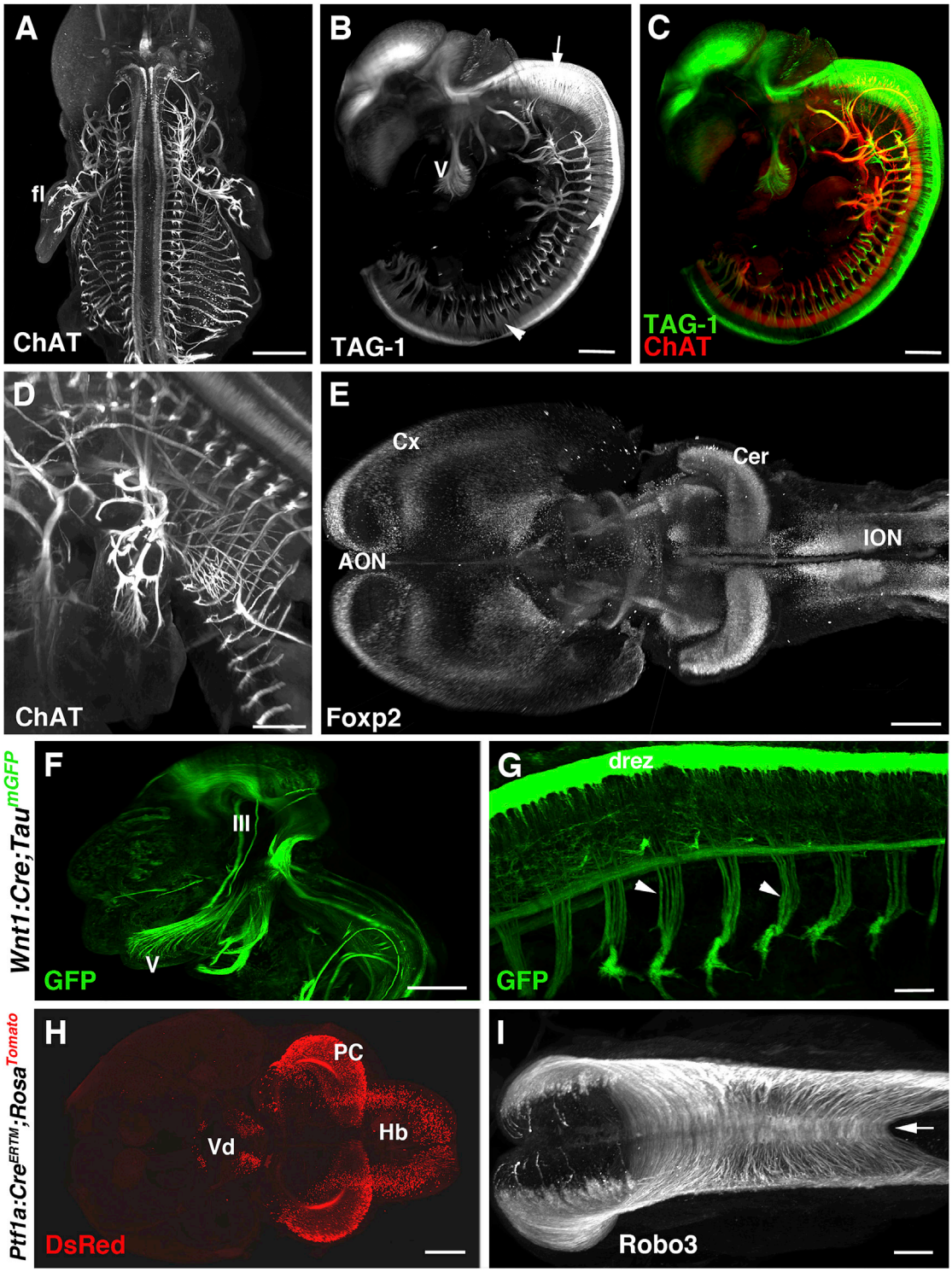

Figure 1. Immunolabeling and 3DISCO Clearing of E11–E13 Embryos

(A–D) E12 mouse embryos labeled with anti-ChAT (A, C, and D) and anti-TAG-1 (B and C) antibodies. (A) Ventral view of the spinal cord motor columns and the motor projections in the rib cage and forelimbs (fl). (B and C) Side view. TAG-1 (B) labels sensory projections in the periphery, such as the trigeminal nerve (V) and dorsal root ganglia (arrowheads), and commissural axons in the hindbrain and spinal cord (arrow). (C) Overlay of ChAT and TAG-1 immunostaining. (D) High magnification of motor innervation in the forelimb.

(E) Ventral view of the brain of an E13 embryo labeled with anti-Foxp2 antibodies. The entire expression pattern of FoxP2+ neurons can be observed in a single brain. Foxp2 is highly expressed in the inferior olivary nucleus (ION), Purkinje cells in the cerebellum (Cer), neocortex (Cx), and anterior olfactory nucleus (AON).

(legend continued on next page)

RESULTS

Immunolabeling of Mouse Embryos Is Compatible with 3DISCO Clearing

First, we tested the technique on embryonic day 12 (E12)–E14 mouse embryos immunostained with antibodies against choline acetyl transferase (ChAT) to label motor projections and transient axonal glycoprotein 1 (TAG-1/Contactin-2), which is expressed by many axons (Yamamoto et al., 1986), including sensory ganglia axons (Figures 1A–1D). The precise 3D pattern of motor and sensory projections could be visualized, including oculomotor nerves and limb innervation (Movies S1, S2, and S3). Postacquisition treatments using Imaris allowed us to obtain high-resolution images of regions of interest. The samples, or part of it, such as a limb (Figure 1D; Movie S4), could be optically sliced in all orientations, thereby allowing one to generate classic sagittal, horizontal, and coronal sections with a single embryo. Next, we used anti-FoxP2 (forkhead box P2) antibody, which recognizes a transcription factor expressed by neurons in multiple brain areas (Ferland et al., 2003; Fujita and Sugihara, 2012). The comprehensive distribution of FoxP2 immunoreactive nuclei was revealed (Figure 1E). Notably, automatic 3D counting of the number of FoxP2+ neurons could also be done (data not shown).

Transgenic mice expressing fluorescent proteins are increasingly used to study axonal circuits and gene expression patterns. To determine if the quenching of fluorescent proteins after 3DISCO could be overcome by antibody staining, we performed anti-GFP staining. *Tau-lox-Stop-lox-mGFP-IRES-nls-lacZ* mice (Tau^{mGFP}), which express a membrane-tethered GFP in axons following Cre-mediated recombination (Hippenmeyer et al., 2005), were crossed with *Wnt1:Cre* mice. In this line, Cre recombinase is targeted to some hindbrain and spinal cord commissural neurons and sensory ganglia (Danielian et al., 1997). In E11.5 *Wnt1:Cre;*Tau^{GFP} embryos, GFP-immunoreactive axons could be followed throughout the CNS and peripheral nervous system (Figures 1F and 1G; Figure S1A; Movies S5 and S6). Likewise, anti-dsRed immunostaining was performed on E14 *Ptf1a:*Cre^{ERTM};$Rosa26^{dTomato}$ embryos that had received tamoxifen at E12.5. In this line, Cre is activated upon tamoxifen injection in subsets of neurons in the CNS (Kopinke et al., 2012), and this induces the expression of a red fluorescent protein from the Tomato transgene inserted into the ubiquitous *Rosa* locus (Madisen et al., 2010). After anti-dsRed immunostaining and clearing, the distribution of Tomato-positive neurons, derived from Ptf1a+ progenitors, could be observed, including Purkinje cells in the cerebellum (Figure 1H). This showed that 3DISCO, in combination with immunostaining, can bypass the problem of native fluorescence instability. Last, we performed immunostaining against Robo3, a transmembrane receptor of the roundabout family, transiently expressed by commissural axons in the mouse hindbrain and spinal cord (Marillat et al., 2002; Sabatier et al., 2004). In the E11 spinal cord, the whole array of commissural axons crossing the floor plate was observed in the spinal cord and hindbrain (Figure 1I; Figure S1B; Movies S7 and S8).

Robo3 Is a Selective Marker of the Fasciculus Retroflexus

We next performed whole-mount anti-TAG1 immunostaining on E16 brain and could observe that the 3D framework of TAG-1+ axons such as the lateral olfactory tract, anterior commissure, and commissural axons in the hindbrain (Figure 2A). By contrast, at E16, Robo3 was still detected in the hindbrain, such as in late-migrating pontine neurons, but it was absent from the forebrain (Figure 2B; Movie S9). Surprisingly, only the FR was immunoreactive for Robo3 in the diencephalon (Figures 2B–2E). Robo3 was only expressed in the mHb, as previously described (Quina et al., 2009; Schmidt et al., 2014; data not shown). FR axons cross multiple times and zigzag at the ventral midline (Ramon y Cajal, 1911; Iwahori et al., 1993 ; Bianco et al., 2008). This feature was seen on 3D images and following optical slicing (Figure 2E; Movie S10). The presence of Robo3 in E16 FR axons, which reach the ventral midline around E13–E14 (Funato et al., 2000), was unexpected, as this receptor is usually downregulated in postcrossing axons (Marillat et al., 2002; Sabatier et al., 2004). Tissues shrink after clearing with 3DISCO (Ertürk and Bradke, 2013), but the FR length (Figure S1C) was similar between E16 brains (862.9 μm ± 10.5 SEM; n = 20 E16 brains; p = 0.93; one-sample t test). It was also equivalent between the right (867.1 μm ± 14.8 SEM) and left (858.7 μm ± 15.3 SEM; p = 0.34; paired t test) side. This demonstrates that the shrinkage is homothetic and that comparing relative dimensions between cases is possible. Although LSM is the most rapid and efficient method to image cleared samples (see also Tomer et al., 2014), confocal microcopy could be used (Figure S1D). Lastly, the same sample could be imaged several times without significant quenching of the fluorescence, which was only slightly diminished 6 months after clearing (Figure S1E). We next attempted to perform whole–mount Robo3 immunostaining and 3DISCO clearing on postnatal brain (postnatal day 0 [P0] and P5). This revealed that FR axons still expressed high levels of Robo3 and that no other tracts were labeled in the CNS (Figures 2F–2H). However, Robo3 was not expressed in the adult mHb (data not shown). The FR could also be stained with antibodies against the netrin-1 receptor deleted in colorectal cancer (DCC) and TAG-1 (Figures 2J and 2K; Figure S1F), as previously shown (Wolfer et al., 1994; Yamamoto et al., 1986; Funato et al., 2000; Schmidt et al., 2014). Therefore, we next studied FR structure in a collection of knockout mice for axon guidance molecules involved in midline crossing.

(F and G) Side views of an E11.5 *Wnt1:Cre;*Tau^{mGFP} embryo labeled with anti-GFP. The oculomotor nerve (III) and trigeminal axons (V) are seen in (F). (G) High magnification of the spinal cord showing axons from dorsal root ganglia neurons (arrowheads) and the dorsal root entry zone (drez).

(H) Dorsal view of the brain an E14 *Ptf1a:*Cre^{ERTM};$Rosa^{Tomato}$ embryo injected with tamoxifen at E12.5 and immunostained with anti-dsRed. The distribution of Tomato+ neurons originating from E12.5 Ptf1a+ progenitors is seen, including a subset of cerebellar Purkinje cells (PC), cells in the hindbrain (Hb), and ventral diencephalon (Vd).

(I) Dorsal view of the spinal cord of an E11 mouse embryo stained with anti-Robo3 antibodies. The commissural axons are seen crossing the floor plate (arrow). Scale bars represent 100 μm (I), 150 μm (G), 200 μm (D), 300 μm (E and H), 400 μm (A–C), and 600 μm (F).

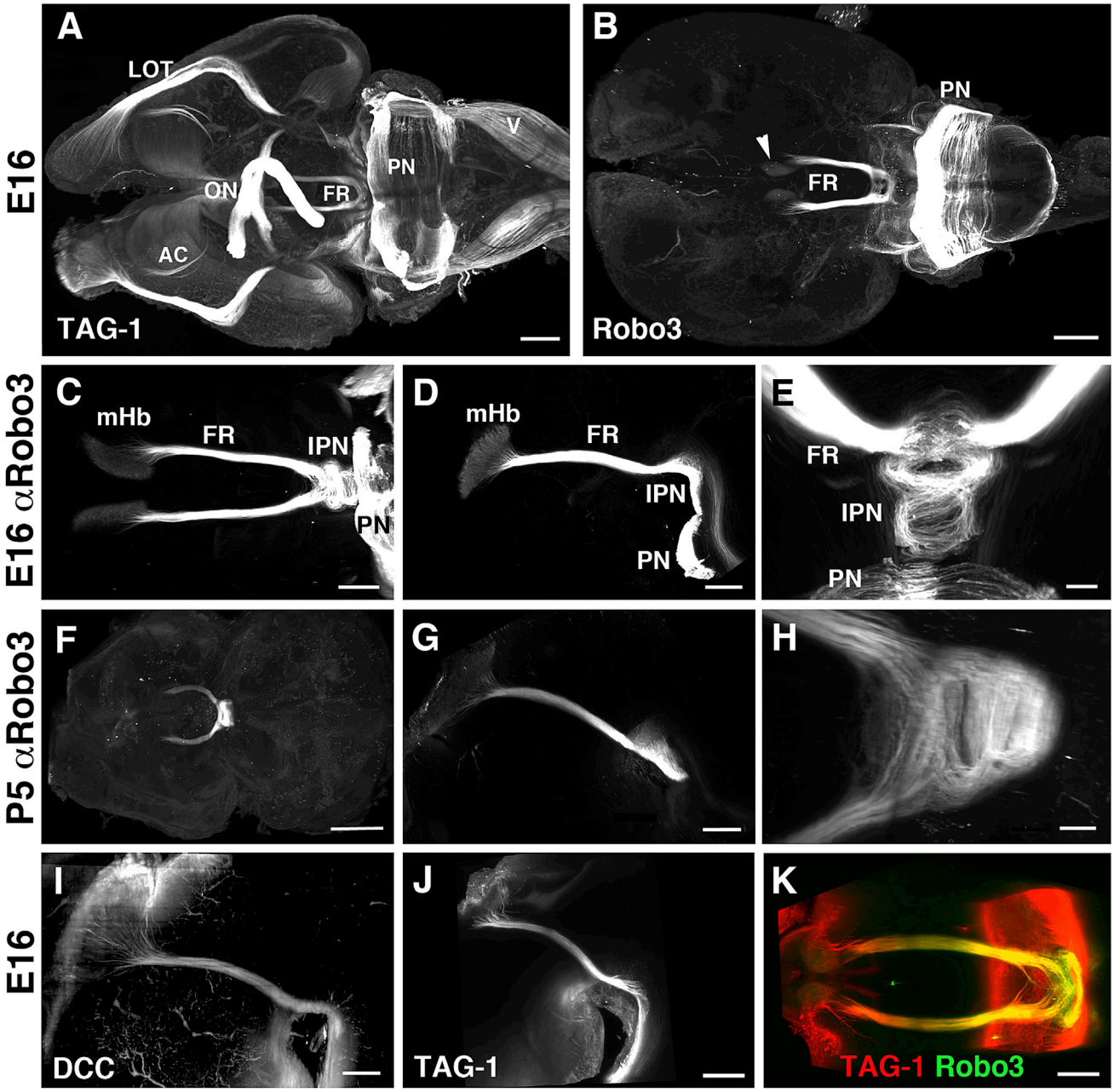

Figure 2. Robo3 Labeling and 3DISCO Clearing Is a Unique Tool to Study the Development of the Fasciculus Retroflexus

(A) Ventral view of an E16 brain stained with anti-TAG-1. TAG-1 is expressed in the lateral olfactory tract (LOT), anterior commissure (AC), optic nerve (ON), fasciculus retroflexus (FR), pontine neurons (PN), and trigeminal axons (V).

(B) Ventral view of an E16 brain stained with anti-Robo3. Migrating pontine neurons (PN) are seen in the hindbrain, and only the FR is labeled in the diencephalon. The arrowhead indicates the medial habenula.

(C–E) Robo3 immunostaining of the FR of an E16 embryo in ventral (C), lateral (D), and caudal (E) views. Axons from the medial habenula (mHb) project via the FR to the interpeduncular nucleus (IPN). Pontine neurons (PN) also express Robo3.

(F–H) Robo3 immunostaining on a P5 brain. The FR is the only tract labeled. Dorsal view (F), lateral view (G), and higher magnification of the IPN level (H) are shown.

(I–K) Lateral (I and J) and dorsal (K) views of the FR of E16 embryos labeled with antibodies against DCC (I), TAG-1 (J), or TAG-1 and Robo3 (K). Note in (K) that FR axons coexpress TAG-1 and Robo3.

Scale bars represent 50 μm (E), 100 μm (K), 150 μm (I), 200 μm (C, D, G, and J), 300 μm (A), and 500 μm (B, F, and H).

3D Analysis of the Development of the FR in Midline Guidance Mutants

Previous studies showed that Netrin-1 attracts FR axons and that the FR is disorganized in *Netrin-1* and *DCC* mutants (Funato et al., 2000; Schmidt et al., 2014). However, the phenotypic analysis of *Netrin-1/DCC* knockout embryos was done on cryostat sections that only provide an incomplete visualization of the guidance defects. Robo3 immunostaining and 3DISCO clearing revealed that the FR was severely perturbed in E16 *DCC* and *Netrin-1* knockout embryos (n = 8 and n = 6, respectively). Interestingly, this method allowed us to compare FR axonal defects between cases and score embryos as done in invertebrate species and zebrafish. In each case, the position and orientation of all the Robo3+ fascicles was determined.

In all *DCC* knockout embryos (n = 8/8), a large axonal bundle projected rostrally from the mHb instead of caudally and a second one grew along the normal pathway to the IPN level (Figures 3D–3I; Movie S11). These axons passed the IPN and extended along the midline. Floor plate crossing was severely reduced in all cases, although a few axons still crossed in six of eight cases (Figure 3F; Figures S2D and S2E). In five of the eight embryos, a small tract projected dorsally from the mHb and aberrant crossing of the dorsal midline at the level of the mHb was observed. Overall, the embryos could be grouped in two main categories (containing five and three embryos, respectively) based on their combination of axonal defects.

Next we studied *Netrin-1* knockout embryos (Figures 3J–3O). The spectrum of Robo3+ FR axon guidance defects was distinct from *DCC* knockouts. Compared to a single tract in wild-type (n = 5/5) and *Netrin-1*$^{+/-}$ (n = 7/7) embryos, the mHb projections were strongly defasciculated in *Netrin-1*$^{-/-}$ embryos (n = 6/6), but cases were heterogeneous. In five out of six *Netrin-1*$^{-/-}$ embryos, a fascicle failed to grow toward the midline and projected caudally from the mHb, and in two out of six cases, a small tract extended rostrally from the mHb (Figures 3J–3O; Movie S12). Like in *DCC* knockouts, dorsal midline crossing was observed (four out of six cases; Figures S2B and S2C). All other axons extended along the normal FR pathway, but one or two large fascicles left the main tract dorsally before the IPN. The remaining axons reached the IPN and formed a commissure (six out of six embryos) from which a few axons extend pass the IPN parallel to the ventral midline (two out of six). In a single embryo (Figures 3M–3O), a fascicle of axons extended ventrorostrally instead of caudally when approaching the IPN. These data show that although a pattern of FR axon guidance defects could established, their combination was almost unique to each embryo. This confirms that Netrin-1 and DCC play a major role in FR axon guidance but indicates that their role is not limited to floor plate crossing.

Habenula neurons and FR axons express Robo1 and Robo2 receptors and Slit ligands (Marillat et al., 2002; Schmidt et al., 2014), but the consequence of *Slit* or *Robo* loss of function on FR development had not been studied. Therefore, we applied our clearing procedure to the analysis of FR organization in *Slit* and *Robo* mutants. In *Robo*$^{-/-}$*;Robo*$^{-/-}$ double knockouts (n = 6), FR axons formed a single tract and reached the IPN (Figures 4A–4C; Movie S13), where they defasciculated into smaller bundles. Some axons crossed the midline, but many remained on the ipsilateral side without extending further caudally (n = 6/6). In only one embryo, a few axons crossed the dorsal midline at the level of the mHb (data not shown). Next, we used anti-Tag1 immunostaining to study the organization of FR projections in *Robo3* knockouts (n = 3). FR axons extended to the IPN level and crossed the floor plate (Figures 4D–4F; Movie S14), but they next turned back toward the midline and coalesced at the midline. Together, the FR wiring defects in *Robo* mutants were unexpected and distinct from what has been described for other commissural tracts (see Discussion). We next studied various combinations of *Slit* knockouts, including a conditional *Slit2*^{lox} allele. To delete Slit2 from the floor plate, *Slit2*^{lox} mice were crossed to the *Shh:Cre* line, in which Cre is highly expressed throughout the floor plate. In *Slit1*$^{-/-}$ knockouts (n = 1) and single and compound heterozygous controls (n = 3), Robo3+ FR axons projected as in wild-type embryos (Figures 4G–4I and data not shown). However, severe midline crossing defects were observed in *Shh:Cre;Slit1*$^{-/-}$*;Slit2*$^{lox/lox}$ and *Shh:Cre;Slit1*$^{-/-}$*;Slit2*$^{lox/lox}$*;Slit3*$^{-/-}$ embryos (n = 2 for each genotype). In both mutants, FR axons projected to the IPN, but their growth at the midline was perturbed. In *Shh:Cre;Slit1*$^{-/-}$*;Slit2*$^{lox/lox}$ embryos, FR axons defasciculated at the IPN level but then followed the floor plate in both directions (Figures 4J–4K; Movie S15) toward the diencephalon or hindbrain. In *Shh:Cre;Slit1*$^{-/-}$*;Slit2*$^{lox/lox}$*;Slit3*$^{-/-}$ embryos, each FR divided into two branches that crossed the midline and joined axons from the contralateral FR to form two commissures. In addition, a bundle of axons escaped the anterior commissure to grow along the ventral midline (Figure 4O; Movie S16). Together, these results show that 3DISCO clearing after whole-mount immunostaining reveals unexpected axonal defect in midline mutants.

DISCUSSION

Whole-Mount Immunostaining and 3DISCO Clearing: An Optimal Recipe for Studying Brain Connectivity?

Embryos from most invertebrate species, such as *Drosophila* or *C. elegans*, or some vertebrates, including zebrafish or *Xenopus*, are optically transparent. Therefore, one can visualize and reconstruct entirely axonal tracts and their arborization using specific transgenes or whole-mount immunostaining. This has facilitated the phenotypic characterization of axon guidance mutants and large-scale genetic screens (Baier et al., 1996; Kolodkin et al., 1993; Seeger et al., 1993; Zallen et al., 1998). By contrast, mammalian embryos and postnatal brains are opaque and current imaging techniques mostly restrict the 3D analysis of axonal connections to young embryos or brain samples at immature stages. Older brains need to be cut, which is time consuming and only provides fragmentary information on brain connectivity. Serial electron microscopy was used to reconstruct neuronal networks in small pieces of tissue (Helmstaedter et al., 2013), but the technique is still in its infancy and inaccessible to most laboratories. Using it for genetic screens or to assess interspecimen variability would also be extremely challenging.

A few forward genetic screens for axon guidance mutants have been performed in mice using N-ethyl-N- nitrosourea mutagenesis (Lewcock et al., 2007; Merte et al., 2010) but restricted to E11.5–E12.5 embryos. We show here that our imaging method is

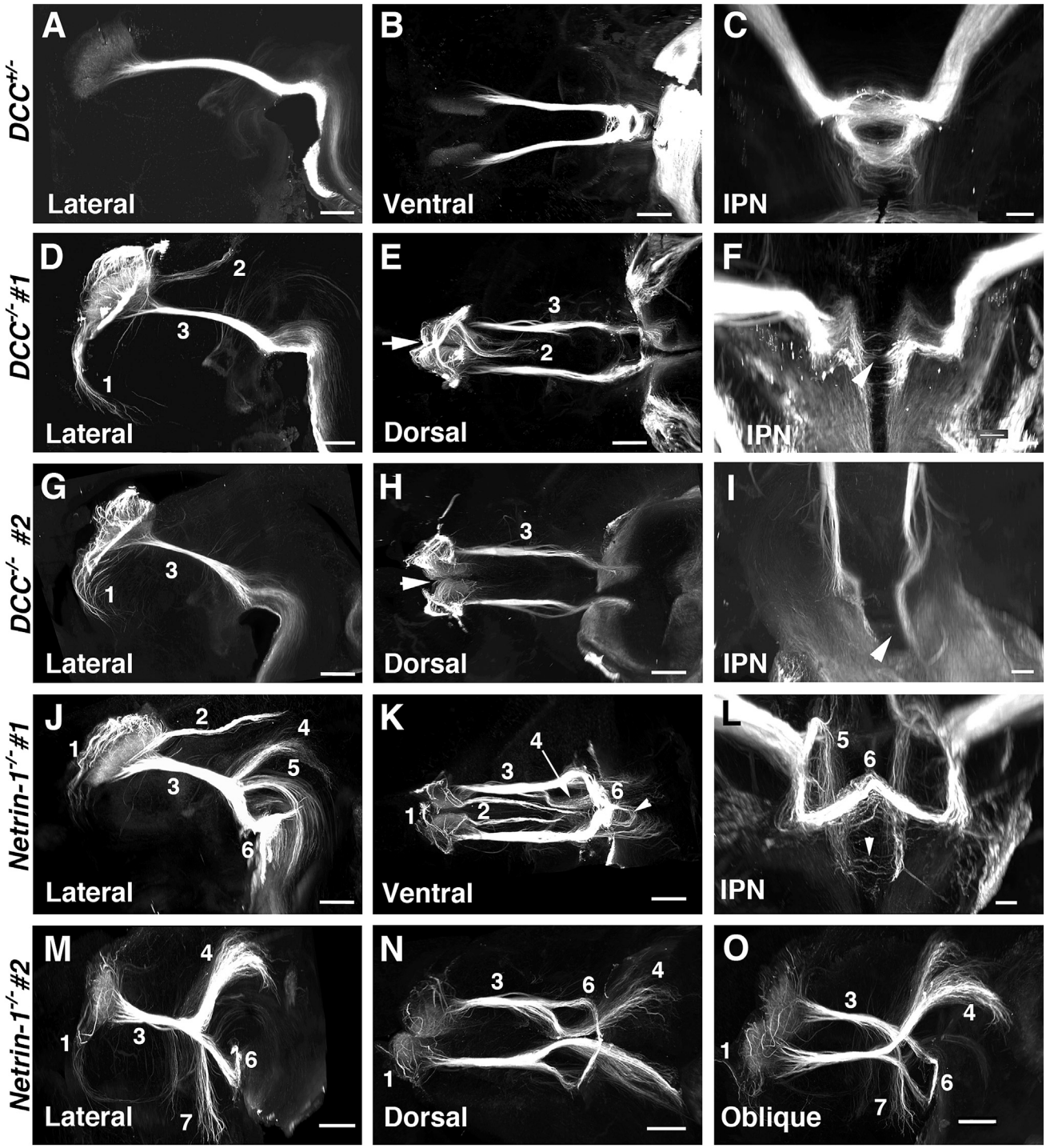

Figure 3. Diversity of FR Axon Guidance Defects in *Netrin-1* and *DCC* Knockouts

Robo3 immunostaining and 3DISCO clearing on E16 $DCC^{+/-}$ (A–C), $DCC^{-/-}$ (D–I), $Netrin\text{-}1^{-/-}$ (J–O) embryos imaged by LSM. Lateral, oblique, ventral, and dorsal views and caudal views at the IPN level (IPN) are shown.

(A–C) Normal FR in a $DCC^{+/-}$ embryo.

(D–F) Organization of FR axons in one $DCC^{-/-}$ mutant (#1). An abnormal tract develops rostrally (1) and another one caudally (2). Other FR axons (3) reach the IPN, but only a few cross the midline (arrowhead in F). Note that many axons cross the dorsal midline at the level of the habenula (arrowhead in E).

(G–I) FR defects in another $DCC^{-/-}$ embryo (#2). The rostral tract is also present (1). Other FR axons reach the IPN (3) but fail to cross the midline (arrowhead in I). Axons do not cross the dorsal midline (arrowhead in H).

(legend continued on next page)

fast, inexpensive, and scalable enough for processing a large number of embryos. Moreover, it is compatible with multiple labeling and therefore several types of axonal tracts can be stained in a single embryo. The procedure is technically simple and does not require any specific device (perfusion is not even needed). Another main advantage of this immunostaining/clearing procedure over existing ones is its low cost (about 10 Euros [€] per sample, including 3€ of antibodies and only 3.5€ of clearing solutions), which can be reduced if several embryos are processed simultaneously. Last, brains and embryos can be stored for weeks before staining and after clearing. As with every immunohistochemical procedure, the staining protocol will have to be optimized for each antibody and specific needs. Our work also confirms that LSM is a very powerful imaging technique for 3D analysis of brain connectivity.

Unique Features of Midline Guidance in the Habenular System

The habenular complex is an important relay between the limbic forebrain and caudal brain nuclei, in particular monoaminergic ones (Herkenham and Nauta, 1979; Hikosaka, 2010). The medial habenula project mostly to the IPN (Kuhar et al., 1975) and plays a role in nicotine intake (Fowler et al., 2011) and anxiety (Yamaguchi et al., 2013), among other emotional behaviors. The habenula has fascinated neuroatomists for being an asymmetric brain structure in most vertebrate species, excepting mammals. This lateralization (in size, neurotransmitter content, and connectivity) is most obvious in anamniotes, including fish (Amo et al., 2010). In zebrafish, the axons from both sides cross the midline multiple times in a different pattern depending on their lateral origin in the dorsal habenula (Bianco et al., 2008). This unusual, and seemingly unique, midline recrossing behavior was also described in mammals (Ramon y Cajal, 1911; Iwahori et al., 1993). This raised the question of the underlying axon guidance mechanisms, as in other commissural systems, midline recrossing is prevented (Chédotal, 2011). We show here that Slit/Robo signaling plays a major role in the control of midline recrossing. Although FR pathfinding to the midline is not affected in *Robo1/2, Robo3* knockouts or in mice lacking all Slit expression at the floor plate, their final arborization is severely perturbed. Midline recrossing is strongly reduced in *Robo1/2* double knockouts. This is somehow counterintuitive, as one would have expected axons to recross or coalesce at the midline, as described in other commissural systems (Farmer et al., 2008; Jaworski et al., 2010). Likewise, the FR phenotype of *Robo3* knockout is unexpected, as axons cross the midline and even fail to leave it. Moreover, Robo3 is still expressed by FR axons several days after they crossed the midline, unlike in other commissural systems (Marillat et al., 2004; Sabatier et al., 2004). The analysis of *Slit* triple knockouts also reveals that Slits control the defasciculation of FR axons at the midline and prevent them from growing caudally and rostrally, thereby confining them to the IPN level.

By contrast, the analysis of *Netrin-1* and *DCC* knockouts demonstrates that they are essential for guiding FR axons to the midline and promoting crossing. However, they also favor FR axon fasciculation and prevent axons from crossing the dorsal midline or from extending rostrally, as previously described (Schmidt et al., 2014). The distinct fascicles that form in these mutants might reflect the molecular diversity of the adult medial habenula (Yamaguchi et al., 2013). This heterogeneity of guidance defects is unlikely to rely on a differential expression of unc5 receptors in mHb neurons, as they only express *unc5a*, and homogeneously (van den Heuvel et al., 2013).

Interestingly, the spectrum of axon defects is specific for each mutant line, and a common signature of pathfinding errors can be established. However, a clear interindividual variability exists in each knockout line. For *Netrin-1* knockouts, this could be related to a hypomorphic allele (Serafini et al., 1996), but this should not be the case for the other mutants. This suggests that FR axon rewiring in these mutant is partially stochastic.

In conclusion, this method will facilitate the development of large-scale forward genetic screens and of 3D atlases of immunolabeled tissues. It will be a valuable tool to implement ongoing initiatives aimed at establishing the brain connectome (see, for instance, http://connectivity.brain-map.org/ and http://www.gensat.org/index.html).

EXPERIMENTAL PROCEDURES

Mouse Strains and Genotyping

Netrin-1 (Serafini et al., 1996), *DCC* (Fazeli et al., 1997), *Robo3* (Sabatier et al., 2004), *Slit1/Slit2* (Plump et al., 2002), *Slit3* (Yuan et al., 2003), *Robo1* (Long et al., 2004), *Robo2* (Grieshammer et al., 2004) and $Slit2^{lox}$ (Gibson et al., 2014) knockouts and *Shh:Cre* (Harfe et al., 2004), $Ptf1a{:}Cre^{ERTM}$ (Kopinke et al., 2012), *Wnt1:Cre* (Danielian et al., 1997), Tau^{GFP} (Hippenmeyer et al., 2005), and *Rosa26:dTomato* (Madisen et al., 2010) lines were previously described and genotyped by PCR. Wild-type mice were from the C57BL6 background (Janvier France). Compound mutants were obtained by intercrossing the various lines. The day of the vaginal plug was counted as E0.5. Postnatal and adult mice were anesthetized with ketamine (100 mg/ml) and xylazine (10 mg/ml).

Embryos were collected at E12, E14, E16, and E18 and transferred to ice-cold PBS 1X (Invitrogen). From E16, the nervous system was dissected and a small hole was made in the telencephalon to facilitate the diffusion of the antibodies. At postnatal ages (P0 to P8), brains were dissected and fixed by immersion in 4% paraformaldehyde (PFA; Merck) for 3 hr at room temperature (RT) or overnight at 4°C. Samples were kept at 4°C in PBS 1X until use.

All animal procedures were carried out in accordance to institutional guidelines (UPMC and INSERM).

(J–L) FR defects in a $Netrin\text{-}1^{-/-}$ mutant (#1). Some axons project rostrally over the medial habenula (1) without crossing the midline, a bundle grow caudally from the habenula (2), and other axons extend along the normal FR pathway (3). Two bundles leave the main tract to project dorsally before reaching the IPN (4 and 5), whereas other axons reach the IPN level. They form a large commissure (6), but a few axons extend more caudally parallel to the floor plate, and only a few cross it (arrowhead in K and L).

(M–O) Distinct FR guidance defects in another $Netrin\text{-}1^{-/-}$ mutant (#2). The dorsal defasciculation at habenula level is also seen (1), but most axons grow along the normal FR pathway (3). Upon reaching the floor plate, a large bundle is deflected dorsally (4) and a smaller ventral fascicle also forms in the ventral diencephalon (7). Other axons reach the IPN level and cross the midline to form a small commissure (6).

Scale bars represent 50 μm (C, F, and L), 100 μm (I), and 200 μm (A, B, D, E, G, H, J, K, and M–O).

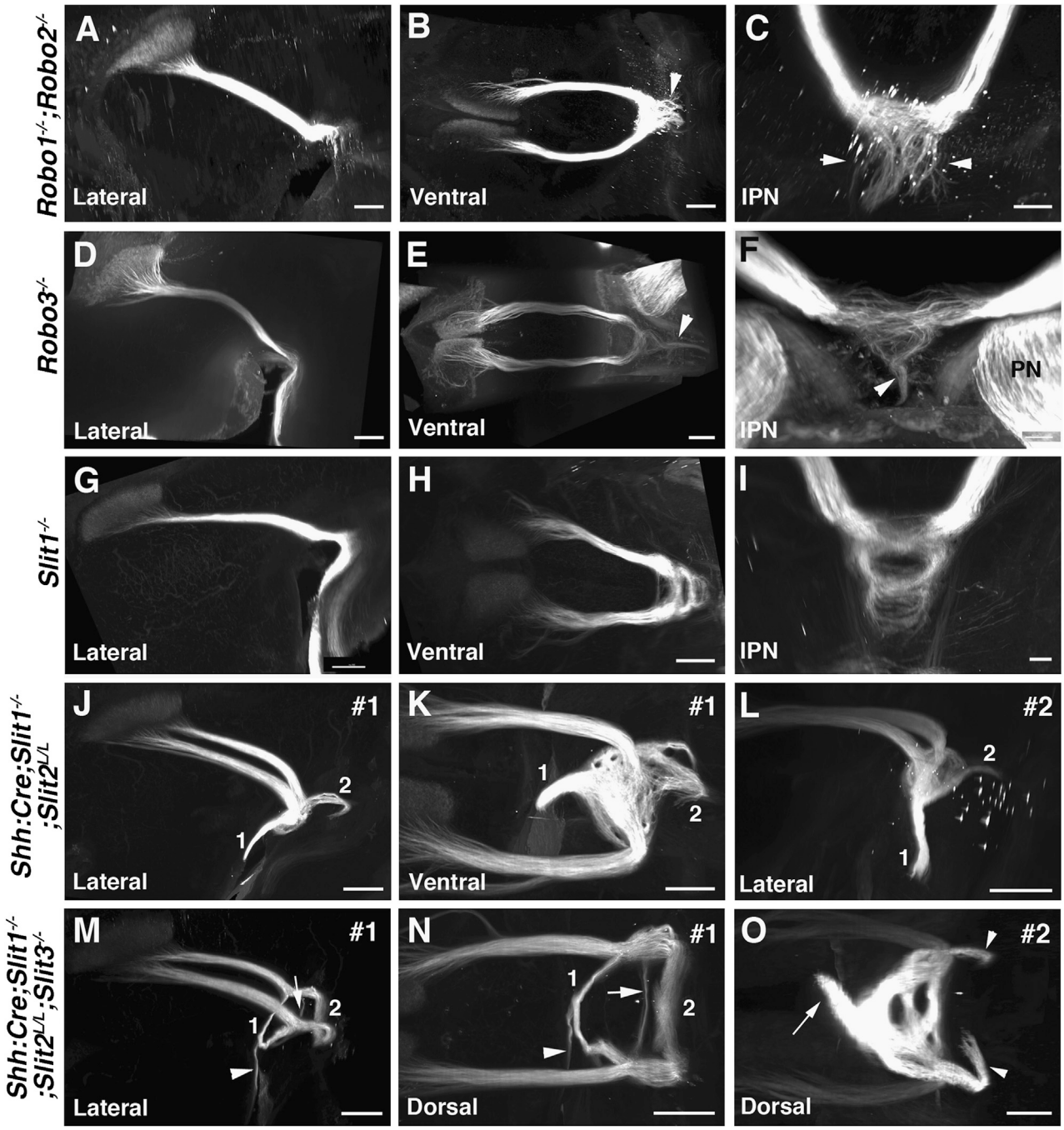

Figure 4. FR Axon Guidance Defects in *Slit* and *Robo* Knockouts

Robo3 (A-C, G-O) or TAG-1 (D–F) immunostaining and 3DISCO clearing in E16 *Slit* and *Robo* mutant embryos.

(A–C) In *Robo1*$^{-/-}$;*Robo2*$^{-/-}$ knockouts, the FR is similar to control until the IPN, where the axons defasciculate (arrowheads in C).

(D–F) In a *Robo3*$^{-/-}$ mutant, the FR reaches the IPN, where they cross the midline and extend caudally within the midline.

(G–I) in *Slit1*$^{-/-}$ embryos, the FR is similar to controls.

(J–L) Two *Shh:Cre;Slit1*$^{-/-}$;*Slit2*$^{lox/lox}$ embryos (#1 and #2). In both cases, FR axons reach the IPN and then form a dense meshwork at the floor plate level from which two axon bundles emerge and extend along the floor plate rostrally (1) and caudally (2).

(M–O) Two *Shh:Cre;Slit1*$^{-/-}$;*Slit2*$^{lox/lox}$;*Slit3*$^{-/-}$ embryos (#1 and #2). Again the FR is comparable to controls until axons reach the floor plate. In one case (#1 in M and N), FR axons from two large commissures: a rostral one (1) and a caudal one (2). A small tract leaves the rostral commissure to grow along the floor plate (arrowheads in M and N). In the second case (O), three commissures are observed, but they are more compact and the anterior medial bundle is larger (arrow). Moreover, two small fascicles extend caudally on both sides (arrowheads).

Scale bars represent 40 μm (F), 50 μm (C and I), 100 μm (O), 150 μm (K), and 200 μm (A, B, D, E, G, H, J, and L–N).

Whole-Mount Immunostaining

The procedure was similar for single and multiple labeling. Samples were first incubated at RT on a rotating shaker in a solution (PBSGT) of PBS 1X containing 0.2% gelatin (Prolabo), 0.5% Triton X-100 (Sigma-Aldrich) and 0.01% thimerosal (Sigma-Aldrich) for 3 hr (E12), 24 hr (E14–E18 and P0), or 48 hr (P5 and P8). Samples were next transferred to PBSGT containing the primary antibodies (Table S1) and placed at 37°C, with rotation at 100 rpm, for 3 days (E12), 1 week (E14, E16, and E18), 10 days (P0), or 14 days (P5 and P8). This was followed by six washes of 30 min in PBSGT at RT. Next, samples were incubated in secondary antibodies (Table S2) diluted in PBSGT overnight (E12–E18) or for 2 days (P0–P8) at 37°C. After six washes of 30 min in PBSGT at RT, samples were stored at 4°C in PBS until clearing.

Tissue Clearing

We used the 3DISCO clearing procedure (Ertürk et al., 2012b) and slightly adapted it to our samples. All incubation steps were performed at RT in a fume hood, on a tube rotator (SB3, Stuart) at 14 rpm, using a 15 ml centrifuge tube (TPP, Dutscher) covered with aluminum foil to avoid contact with light. Samples were first dehydrated in a graded series (50%, 80%, and 100%) of tetrahydroflurane (THF; anhydrous, containing 250 ppm butylated hydroxytoluene inhibitor, Sigma-Aldrich) diluted in H_2O, during 1hr (E12-P0) or 90 min (P5) for each step. This was followed by a delipidation step of 20 min (E12 to P0) or 40 min (P5–P8) in dichloromethane (DCM; Sigma-Aldrich). Samples were transferred to 100% DCM until they have sunk. Finally, samples were cleared overnight in dibenzylether (DBE; Sigma-Aldrich). Samples should be stored in brown glass vial (Rotilabo, Roth) filled with DBE, in the dark and at RT. THF, DCM, and DBE are toxic (gloves must be worn at all steps) and flammable. Waste should be treated and eliminated accordingly. DBE must be stored in glass containers.

Imaging

Ultramicroscopy

3D imaging was primarily performed with an ultramicroscope (LaVision BioTec) using InspectorPro software (LaVision BioTec). The light sheet was generated by a laser (wavelength 488 or 561 nm, Coherent Sapphire Laser, LaVision BioTec) and two cylindrical lenses. A binocular stereomicroscope (MXV10, Olympus) with a 2× objective (MVPLAPO, Olympus) was used at different magnifications (1.6×, 4×, 5×, and 6.3×). Samples were placed in an imaging reservoir made of 100% quartz (LaVision BioTec) filled with DBE and illuminated from the side by the laser light. Different dipping caps were used to image large samples with a high working distance or small samples with a low working distance. Images were acquired with a PCO Edge SCMOS CCD camera (2,560 × 2,160 pixel size, LaVision BioTec). The step size between each image was fixed at 1 μm.

The acquisition time with the ultramicroscope depends on the number of lasers (one side or two sides) used to generate and focus the light sheet. It took only 10 min to image (1,488 sections) the habenula and FR with a single light source. For the entire brain, the two light sources were used and the total acquisition time (1,856 sections) was ~1 hr. Each resulting imaris (.ims) file was ~15 Gb in size at a 1 μm z resolution (16-bit images).

Confocal Microscopy

For imaging with an upright confocal microscope (Olympus FV1000), samples were placed on a glass slide, in a homemade PDMS cuvette (DBE resistant) with a rim of 5 mm (Sylgard 184/Silicone elastomer, Dow Corning). The cuvette was filled with DBE and covered with a glass coverslip. Images were obtained with a 10× objective (Olympus UPlanSApo 10×/0.40 numerical aperture objective Royal Microscopical Society, infinity corrected 0.31 mm working distance). Each individual image (.oif file) was 1.08 Gb from confocal for 1 μm z resolution. The acquisition time was of about 4 hr for the FR and therefore much longer than with an ultramicroscope.

3D Imaging and Image Processing

Images, 3D volume, and movies were generated using Imaris x64 software (version 7.6.1, Bitplane). Stack images were first converted to imaris file (.ims) using ImarisFileConverter. File size was next reduced to 8 bits. 3D reconstruction of the sample was performed using "volume rendering" (Imaris). The sample could be optically sliced in any angle using the "orthoslicer" or "obliqueslicer" tools. Air bubbles and crystals that might form at the surface of the samples could be eliminated using the "surface" tool by creating a mask around the each volume. 3D pictures and movies were generated using the "snapshot" and "animation" tools. Finally, images were cropped and, if required, their brightness was adjusted evenly using Photoshop CS4 (Adobe). Movies legends were generated using iMovie 10.0.2.

Alternatively, movies and 3D analysis could be done with free software such as Vaa3D (http://www.vaa3d.org) or Fiji 3D project plugin (Schindelin et al., 2012). However, the quality of the 3D images was not as good as with Imaris (data not shown).

The distance separating the base of the habenula from the IPN was obtained using the "measurement" tool (Imaris), and statistical analysis was performed with Prism 6 (GraphPad).

SUPPLEMENTAL INFORMATION

Supplemental Information includes two figures, two tables, and 16 movies and can be found with this article online at http://dx.doi.org/10.1016/j.celrep.2014.10.037.

ACKNOWLEDGMENTS

This work was supported by grants from the Fondation pour la Recherche Médicale (Programme équipe FRM; reference DEQ20120323700) and the Agence Nationale de la Recherche (ANR-08-MNP-030) to A.C. It was also performed in the frame of the LABEX LIFESENSES (reference ANR-10-LABX-65) supported by French state funds managed by the ANR within the Investissements d'Avenir programme under reference ANR-11-IDEX-0004-02. F.H. was the recipient of fellowships from the Wings for Life Foundation, the Institute for Research on Paraplegia (IRP), and the DFG. The ultramicroscope was purchased with a grant from the Fédération pour la Recherche sur le Cerveau (FRC, Programme espoir en tête, Rotary). We also thank Dr. Domna Karagogeos for providing one of the anti-TAG-1 antibodies and Dr. Chris Wright for the *Ptf1a:Cre^{ERTM}* line.

Received: September 15, 2014
Revised: October 10, 2014
Accepted: October 14, 2014
Published: November 6, 2014

REFERENCES

Amo, R., Aizawa, H., Takahoko, M., Kobayashi, M., Takahashi, R., Aoki, T., and Okamoto, H. (2010). Identification of the zebrafish ventral habenula as a homolog of the mammalian lateral habenula. J. Neurosci. *30*, 1566–1574.

Baier, H., Klostermann, S., Trowe, T., Karlstrom, R.O., Nüsslein-Volhard, C., and Bonhoeffer, F. (1996). Genetic dissection of the retinotectal projection. Development *123*, 415–425.

Beretta, C.A., Dross, N., Guiterrez-Triana, J.A., Ryu, S., and Carl, M. (2012). Habenula circuit development: past, present, and future. Front Neurosci *6*, 51.

Bianco, I.H., Carl, M., Russell, C., Clarke, J.D., and Wilson, S.W. (2008). Brain asymmetry is encoded at the level of axon terminal morphology. Neural Dev. *3*, 9.

Chédotal, A. (2011). Further tales of the midline. Curr. Opin. Neurobiol. *21*, 68–75.

Chen, H., Bagri, A., Zupicich, J.A., Zou, Y., Stoeckli, E., Pleasure, S.J., Lowenstein, D.H., Skarnes, W.C., Chédotal, A., and Tessier-Lavigne, M. (2000). Neuropilin-2 regulates the development of selective cranial and sensory nerves and hippocampal mossy fiber projections. Neuron *25*, 43–56.

Chung, K., Wallace, J., Kim, S.Y., Kalyanasundaram, S., Andalman, A.S., Davidson, T.J., Mirzabekov, J.J., Zalocusky, K.A., Mattis, J., Denisin, A.K., et al. (2013). Structural and molecular interrogation of intact biological systems. Nature *497*, 332–337.

Danielian, P.S., Echelard, Y., Vassileva, G., and McMahon, A.P. (1997). A 5.5-kb enhancer is both necessary and sufficient for regulation of Wnt-1 transcription in vivo. Dev. Biol. *192*, 300–309.

Dodt, H.U., Leischner, U., Schierloh, A., Jährling, N., Mauch, C.P., Deininger, K., Deussing, J.M., Eder, M., Zieglgänsberger, W., and Becker, K. (2007). Ultramicroscopy: three-dimensional visualization of neuronal networks in the whole mouse brain. Nat. Methods *4*, 331–336.

Ertürk, A., and Bradke, F. (2013). High-resolution imaging of entire organs by 3-dimensional imaging of solvent cleared organs (3DISCO). Exp. Neurol. *242*, 57–64.

Ertürk, A., Mauch, C.P., Hellal, F., Förstner, F., Keck, T., Becker, K., Jährling, N., Steffens, H., Richter, M., Hübener, M., et al. (2012a). Three-dimensional imaging of the unsectioned adult spinal cord to assess axon regeneration and glial responses after injury. Nat. Med. *18*, 166–171.

Ertürk, A., Becker, K., Jährling, N., Mauch, C.P., Hojer, C.D., Egen, J.G., Hellal, F., Bradke, F., Sheng, M., and Dodt, H.U. (2012b). Three-dimensional imaging of solvent-cleared organs using 3DISCO. Nat. Protoc. *7*, 1983–1995.

Farmer, W.T., Altick, A.L., Nural, H.F., Dugan, J.P., Kidd, T., Charron, F., and Mastick, G.S. (2008). Pioneer longitudinal axons navigate using floor plate and Slit/Robo signals. Development *135*, 3643–3653.

Fazeli, A., Dickinson, S.L., Hermiston, M.L., Tighe, R.V., Steen, R.G., Small, C.G., Stoeckli, E.T., Keino-Masu, K., Masu, M., Rayburn, H., et al. (1997). Phenotype of mice lacking functional Deleted in colorectal cancer (Dcc) gene. Nature *386*, 796–804.

Ferland, R.J., Cherry, T.J., Preware, P.O., Morrisey, E.E., and Walsh, C.A. (2003). Characterization of Foxp2 and Foxp1 mRNA and protein in the developing and mature brain. J. Comp. Neurol. *460*, 266–279.

Figdor, M.C., and Stern, C.D. (1993). Segmental organization of embryonic diencephalon. Nature *363*, 630–634.

Fowler, C.D., Lu, Q., Johnson, P.M., Marks, M.J., and Kenny, P.J. (2011). Habenular α5 nicotinic receptor subunit signalling controls nicotine intake. Nature *471*, 597–601.

Fujita, H., and Sugihara, I. (2012). FoxP2 expression in the cerebellum and inferior olive: development of the transverse stripe-shaped expression pattern in the mouse cerebellar cortex. J. Comp. Neurol. *520*, 656–677.

Funato, H., Saito-Nakazato, Y., and Takahashi, H. (2000). Axonal growth from the habenular nucleus along the neuromere boundary region of the diencephalon is regulated by semaphorin 3F and netrin-1. Mol. Cell. Neurosci. *16*, 206–220.

Gibson, D.A., Tymanskyj, S., Yuan, R.C., Leung, H.C., Lefebvre, J.L., Sanes, J.R., Chédotal, A., and Ma, L. (2014). Dendrite self-avoidance requires cell-autonomous slit/robo signaling in cerebellar purkinje cells. Neuron *81*, 1040–1056.

Grieshammer, U., Le Ma, Plump, A.S., Wang, F., Tessier-Lavigne, M., and Martin, G.R. (2004). SLIT2-mediated ROBO2 signaling restricts kidney induction to a single site. Dev. Cell *6*, 709–717.

Hama, H., Kurokawa, H., Kawano, H., Ando, R., Shimogori, T., Noda, H., Fukami, K., Sakaue-Sawano, A., and Miyawaki, A. (2011). Scale: a chemical approach for fluorescence imaging and reconstruction of transparent mouse brain. Nat. Neurosci. *14*, 1481–1488.

Harfe, B.D., Scherz, P.J., Nissim, S., Tian, H., McMahon, A.P., and Tabin, C.J. (2004). Evidence for an expansion-based temporal Shh gradient in specifying vertebrate digit identities. Cell *118*, 517–528.

Helmstaedter, M., Briggman, K.L., Turaga, S.C., Jain, V., Seung, H.S., and Denk, W. (2013). Connectomic reconstruction of the inner plexiform layer in the mouse retina. Nature *500*, 168–174.

Herkenham, M., and Nauta, W.J. (1979). Efferent connections of the habenular nuclei in the rat. J. Comp. Neurol. *187*, 19–47.

Hikosaka, O. (2010). The habenula: from stress evasion to value-based decision-making. Nat. Rev. Neurosci. *11*, 503–513.

Hippenmeyer, S., Vrieseling, E., Sigrist, M., Portmann, T., Laengle, C., Ladle, D.R., and Arber, S. (2005). A developmental switch in the response of DRG neurons to ETS transcription factor signaling. PLoS Biol. *3*, e159.

Iwahori, N., Nakamura, K., and Kameda, S. (1993). Terminal patterns of the fasciculus retroflexus in the interpeduncular nucleus of the mouse: a Golgi study. Anat. Embryol. (Berl.) *187*, 523–528.

Jaworski, A., Long, H., and Tessier-Lavigne, M. (2010). Collaborative and specialized functions of Robo1 and Robo2 in spinal commissural axon guidance. J. Neurosci. *30*, 9445–9453.

Ke, M.T., Fujimoto, S., and Imai, T. (2013). SeeDB: a simple and morphology-preserving optical clearing agent for neuronal circuit reconstruction. Nat. Neurosci. *16*, 1154–1161.

Kolodkin, A.L., Matthes, D.J., and Goodman, C.S. (1993). The semaphorin genes encode a family of transmembrane and secreted growth cone guidance molecules. Cell *75*, 1389–1399.

Kopinke, D., Brailsford, M., Pan, F.C., Magnuson, M.A., Wright, C.V., and Murtaugh, L.C. (2012). Ongoing Notch signaling maintains phenotypic fidelity in the adult exocrine pancreas. Dev. Biol. *362*, 57–64.

Kuhar, M.J., DeHaven, R.N., Yamamura, H.I., Rommel-Spacher, H., and Simon, J.R. (1975). Further evidence for cholinergic habenulo-interpeduncular neurons: pharmacologic and functional characteristics. Brain Res. *97*, 265–275.

Lewcock, J.W., Genoud, N., Lettieri, K., and Pfaff, S.L. (2007). The ubiquitin ligase Phr1 regulates axon outgrowth through modulation of microtubule dynamics. Neuron *56*, 604–620.

Long, H., Sabatier, C., Ma, L., Plump, A., Yuan, W., Ornitz, D.M., Tamada, A., Murakami, F., Goodman, C.S., and Tessier-Lavigne, M. (2004). Conserved roles for Slit and Robo proteins in midline commissural axon guidance. Neuron *42*, 213–223.

Madisen, L., Zwingman, T.A., Sunkin, S.M., Oh, S.W., Zariwala, H.A., Gu, H., Ng, L.L., Palmiter, R.D., Hawrylycz, M.J., Jones, A.R., et al. (2010). A robust and high-throughput Cre reporting and characterization system for the whole mouse brain. Nat. Neurosci. *13*, 133–140.

Marillat, V., Cases, O., Nguyen-Ba-Charvet, K.T., Tessier-Lavigne, M., Sotelo, C., and Chédotal, A. (2002). Spatiotemporal expression patterns of slit and robo genes in the rat brain. J. Comp. Neurol. *442*, 130–155.

Marillat, V., Sabatier, C., Failli, V., Matsunaga, E., Sotelo, C., Tessier-Lavigne, M., and Chédotal, A. (2004). The slit receptor Rig-1/Robo3 controls midline crossing by hindbrain precerebellar neurons and axons. Neuron *43*, 69–79.

Merte, J., Wang, Q., Vander Kooi, C.W., Sarsfield, S., Leahy, D.J., Kolodkin, A.L., and Ginty, D.D. (2010). A forward genetic screen in mice identifies Sema3A(K108N), which binds to neuropilin-1 but cannot signal. J. Neurosci. *30*, 5767–5775.

Plump, A.S., Erskine, L., Sabatier, C., Brose, K., Epstein, C.J., Goodman, C.S., Mason, C.A., and Tessier-Lavigne, M. (2002). Slit1 and Slit2 cooperate to prevent premature midline crossing of retinal axons in the mouse visual system. Neuron *33*, 219–232.

Quina, L.A., Wang, S., Ng, L., and Turner, E.E. (2009). Brn3a and Nurr1 mediate a gene regulatory pathway for habenula development. J. Neurosci. *29*, 14309–14322.

Ramon y Cajal, S. (1911). Histologie Système Nerveux de L'homme et des Vertébrés, *Vol 2* (Paris: Maloine).

Sabatier, C., Plump, A.S., Le Ma, Brose, K., Tamada, A., Murakami, F., Lee, E.Y., and Tessier-Lavigne, M. (2004). The divergent Robo family protein rig-1/Robo3 is a negative regulator of slit responsiveness required for midline crossing by commissural axons. Cell *117*, 157–169.

Sahay, A., Molliver, M.E., Ginty, D.D., and Kolodkin, A.L. (2003). Semaphorin 3F is critical for development of limbic system circuitry and is required in neurons for selective CNS axon guidance events. J. Neurosci. *23*, 6671–6680.

Schindelin, J., Arganda-Carreras, I., Frise, E., Kaynig, V., Longair, M., Pietzsch, T., Preibisch, S., Rueden, C., Saalfeld, S., Schmid, B., et al. (2012). Fiji: an open-source platform for biological-image analysis. Nat. Methods *9*, 676–682.

Schmidt, E.R., Brignani, S., Adolfs, Y., Lemstra, S., Demmers, J., Vidaki, M., Donahoo, A.L., Lilleväli, K., Vasar, E., Richards, L.J., et al. (2014). Subdomain-mediated axon-axon signaling and chemoattraction cooperate to regulate afferent innervation of the lateral habenula. Neuron *83*, 372–387.

Seeger, M., Tear, G., Ferres-Marco, D., and Goodman, C.S. (1993). Mutations affecting growth cone guidance in Drosophila: genes necessary for guidance toward or away from the midline. Neuron *10*, 409–426.

Serafini, T., Colamarino, S.A., Leonardo, E.D., Wang, H., Beddington, R., Skarnes, W.C., and Tessier-Lavigne, M. (1996). Netrin-1 is required for commissural axon guidance in the developing vertebrate nervous system. Cell *87*, 1001–1014.

Susaki, E.A., Tainaka, K., Perrin, D., Kishino, F., Tawara, T., Watanabe, T.M., Yokoyama, C., Onoe, H., Eguchi, M., Yamaguchi, S., et al. (2014). Whole-brain imaging with single-cell resolution using chemical cocktails and computational analysis. Cell *157*, 726–739.

Tomer, R., Ye, L., Hsueh, B., and Deisseroth, K. (2014). Advanced CLARITY for rapid and high-resolution imaging of intact tissues. Nat. Protoc. *9*, 1682–1697.

van den Heuvel, D.M., Hellemons, A.J., and Pasterkamp, R.J. (2013). Spatio-temporal expression of repulsive guidance molecules (RGMs) and their receptor neogenin in the mouse brain. PLoS ONE *8*, e55828.

Wolfer, D.P., Henehan-Beatty, A., Stoeckli, E.T., Sonderegger, P., and Lipp, H.P. (1994). Distribution of TAG-1/axonin-1 in fibre tracts and migratory streams of the developing mouse nervous system. J. Comp. Neurol. *345*, 1–32.

Yamaguchi, T., Danjo, T., Pastan, I., Hikida, T., and Nakanishi, S. (2013). Distinct roles of segregated transmission of the septo-habenular pathway in anxiety and fear. Neuron *78*, 537–544.

Yamamoto, M., Boyer, A.M., Crandall, J.E., Edwards, M., and Tanaka, H. (1986). Distribution of stage-specific neurite-associated proteins in the developing murine nervous system recognized by a monoclonal antibody. J. Neurosci. *6*, 3576–3594.

Yang, B., Treweek, J.B., Kulkarni, R.P., Deverman, B.E., Chen, C.K., Lubeck, E., Shah, S., Cai, L., and Gradinaru, V. (2014). Single-cell phenotyping within transparent intact tissue through whole-body clearing. Cell *158*, 945–958.

Yuan, W., Rao, Y., Babiuk, R.P., Greer, J.J., Wu, J.Y., and Ornitz, D.M. (2003). A genetic model for a central (septum transversum) congenital diaphragmatic hernia in mice lacking Slit3. Proc. Natl. Acad. Sci. USA *100*, 5217–5222.

Zallen, J.A., Yi, B.A., and Bargmann, C.I. (1998). The conserved immunoglobulin superfamily member SAX-3/Robo directs multiple aspects of axon guidance in C. elegans. Cell *92*, 217–227.